



JGR Space Physics

RESEARCH ARTICLE

10.1029/2024JA032443

Key Points:

- A physics-based plasma model and a radio propagation model are used to examine the effects of precipitation on auroral scintillation
- Precipitation fluxes with higher energy, a turbulent noise spectrum, and a faster-moving arc intensify scintillation
- The presence of small-scale precipitation amplifies both phase and amplitude scintillations

Supporting Information:

Supporting Information may be found in the online version of this article.

Correspondence to:

P. R. Vaggu, pralayrajvaggu@gmail.com

Citation:

Vaggu, P. R., Zettergren, M., Deshpande, K., Nishimura, Y., Semeter, J., Hirsch, M., et al. (2024). Model-based investigation of electron precipitation-driven density structures and their effects on auroral scintillation. *Journal of Geophysical Research: Space Physics*, 129, e2024IA032443. https://doi.org/10.1029/2024JA032443

Received 11 JAN 2024 Accepted 17 JUN 2024

Model-Based Investigation of Electron Precipitation-Driven Density Structures and Their Effects on Auroral Scintillation

Pralay Raj Vaggu¹, Matt Zettergren¹, Kshitija Deshpande¹, Yukitoshi Nishimura², Joshua Semeter², Michael Hirsch², Don Hampton³, Leslie Lamarche⁴, and Seebany Datta-Barua⁵

¹Department of Physical Sciences, Embry-Riddle Aeronautical University, Daytona Beach, FL, USA, ²Department of Electrical and Computer Engineering and Center for Space Physics, Boston University, Boston, MA, USA, ³Geophysical Institute, University of Alaska, Fairbanks, AK, USA, ⁴Center for Geospace Studies, SRI International, Menlo Park, CA, USA, ⁵Illinois Institute of Technology, Chicago, IL, USA

Abstract Electron density irregularities in the ionosphere can give rise to scintillations, affecting radio wave phase and amplitude. While scintillations in the cusp and polar cap regions are commonly associated with mesoscale density inhomogeneities and/or shearing, the auroral regions exhibit a strong correlation between scintillation and density structures generated by electron precipitation (arcs). We aim to examine the impact of electron precipitation on the formation of scintillation-producing density structures using a high-resolution physics-based plasma model, the "Geospace Environment Model of Ion-Neutral Interactions," coupled with a radio propagation model, the "Satellite-beacon Ionospheric-scintillation Global Model of the upper Atmosphere." Specifically, we explore the effects of varying spatial and temporal characteristics of the precipitation, including electron total energy flux and their characteristic energies, obtained from the all-sky-imagers and Poker Flat Incoherent Scatter Radar observations, on auroral scintillation. To capture small-scale structures, we incorporate a power-law turbulence spectrum that induces short wavelength features sensitive to scintillation. Finally, we compare our simulated scintillation results with satellite-observed scintillations, along with spectral comparisons.

1. Introduction

The influx of energetic particles (particle precipitation) from the magnetosphere into the ionosphere following solar activity is an important production mechanism for ionospheric density irregularities. These irregularities are localized variations in the electron density of the ionosphere, which can lead to disruptions in radio wave propagation and communication. Rapid fluctuations in the trans-ionospheric radio signals are referred to as ionospheric scintillation. Scintillation can degrade the performance of satellite communication links, disrupt Global Positioning System (GPS) signals, and affect radar signal propagation. Understanding and predicting ionospheric scintillation events are important for developing techniques to mitigate their impacts on these systems. At high latitudes, GPS scintillation is attributed to ionospheric irregularities (on the scale of tens of kilometers down to hundreds of meters at GPS frequencies) and gradients in total electron content (TEC) that are typically associated with geomagnetic storms and substorms. Jayachandran et al. (2009, 2012) has reported that the GPS TEC variations are associated with a polar cap arc. The specific mechanisms linking these ionospheric structures to GPS scintillation events are still an area of active research, and the dynamic nature of the highlatitude ionosphere adds to the complexity. The main high-latitude regions exhibiting scintillation are the ionospheric cusp, the polar cap, and the auroral regions. Observational studies have shown that the dominant factors in the production of ionospheric irregularities are plasma flow, density structures, and energetic particle precipitation (Aarons et al., 2000; Hosokawa et al., 2014; Jin et al., 2014; Moen et al., 2013; Weber et al., 1984). This study explores the role electron precipitation plays in structuring the auroral ionosphere, thereby producing the density irregularities that cause auroral scintillation.

1.1. Scintillation Associated With Auroral Activity

Active auroral arcs, characterized by intense and dynamic auroral emissions, often exhibit enhanced scintillation effects on trans-ionospheric radio signals. During active auroral arcs, energetic particles precipitate into the ionosphere, leading to the formation of density structures associated with spatial and temporal variations in the precipitation pattern. These irregularities can cause fluctuations in the phase and/or amplitude of trans

© 2024. American Geophysical Union. All Rights Reserved.

VAGGU ET AL. 1 of 19

ionospheric radio signals, resulting in scintillation. The scintillation effects associated with auroral arcs are typically more pronounced when the arcs exhibit increased brightness and enhanced dynamics, including particle precipitation, plasma instabilities, and field-aligned currents. The complex interplay between these factors contributes to the generation and evolution of the irregularities, thereby influencing the scintillation effects. A basic correlation exists between the brightness of auroral features, specifically arcs, and the intensity of scintillations. Brighter auroral arcs are often associated with stronger scintillation effects (Kintner et al., 2007; Mrak et al., 2018; Semeter et al., 2017; Wang et al., 2021). This correlation suggests that the characteristics and dynamics of the auroral features, such as energy flux, velocity, and scale sizes present in the arc, contribute to generating density irregularities that cause scintillation. Many studies have demonstrated connections between energetic electron precipitation and the presence of small-scale plasma density structures (Kelley et al., 1982). The presence of E-region ionization enhancements concurrent with phase scintillation has been documented by Chartier et al. (2016) and Loucks et al. (2017). Datta-Barua et al. (2015) has shown concurrence between scintillation and soft electron precipitation as evidenced by auroral 630 nm emission and strong F-region plasma heating. Correlations between precipitation and scintillation have been cataloged in the form of a multi-year record of scintillation events using Poker Flat Incoherent Scatter Radar (PFISR) (Sreenivash et al., 2020) and a colocated GPS array Scintillation Auroral GPS Array (SAGA). Collectively, these investigations demonstrate a consistent association between intense energetic electron fluxes and occurrences of auroral scintillation.

1.2. Energy and Spatial Distributions of Energetic Electron Precipitation in Auroral Arcs

The energy distribution of electrons within auroral arcs is crucially important to understand auroral scintillation. The specific energy distribution within the arcs significantly influences the characteristics of these density irregularities and, consequently, the intensity of scintillation. Mathematical functions, such as the Maxwellian, Kappa, and Power law distributions, are used to describe the energy distribution of auroral arcs. The energy spectra of precipitating electrons are well-captured by kappa distributions with energies around a few hundred eV. Conversely, inside strong auroral arcs, a sum of a Maxwellian distribution (for lower energies) and a power law distribution (for higher energies) provide a better fit to the observed spectrum (Ogasawara et al., 2006). In addition, the spectrum shape can also be used to determine the type of aurora with which it is associated. It is generally accepted that accelerated Maxwellian distributions adequately describe the energy spectra of electrons responsible for discrete auroral arcs. At the same time, those associated with diffuse auroras typically adhere to simple Maxwellian distributions (Evans, 1974; Kaeppler et al., 2014; Karlsson, 2012; McIntosh & Anderson, 2014). Nevertheless, it is crucial to note that a certain deviation from the Maxwellian distribution (either accelerated or non-accelerated) more or less exists at higher energies (as depicted in Figure 2 of Morooka et al. (2004)), which can be represented by power-law distributions. Notably, a combination of a Maxwellian distribution at lower energies and a power law distribution at higher energies indicates the presence of both lowenergy and high-energy electrons within the arcs. These different energy populations have distinct effects on the ionospheric plasma and the formation of irregularities.

Regardless of spatial and time structure, high- and low-energy electrons differ in the altitude of the energy deposition. for example, 300 eV electrons deposit energy near the F-region while 5 keV electrons penetrate the mid/lower E-region. Understanding the energy distribution of electrons within auroral arcs allows us to model the formation of density irregularities more accurately, which is essential for predicting and mitigating the impact of scintillation on radio signals in auroral regions. In this study, we represent the precipitating electron energy distribution using a Maxwellian; the spatial structure at mesoscale sizes is taken to be an auroral arc representative of that seen in an event that motivates our model. The smaller-scale (below 4 km) structures are modeled as noiselike power law spectra intended to plausibly mimic the range of small-scale structures from events similar to the one we present.

1.3. Motivation

Understanding the underlying physics behind auroral scintillation and the formation of irregularities is a challenging task. The complexity arises from the simultaneous occurrence of multiple physical processes within a single auroral structure, encompassing strong flow structures, field-aligned currents, and particle precipitation spanning a wide range of energies. In principle, energetic electrons have the potential to generate density irregularities through impact ionization if the precipitation exhibits adequate spatial structure. Additionally, these electrons can establish persistent seed structures, subsequently leading to further structuring through instabilities

VAGGU ET AL. 2 of 19

(Kintner & Seyler, 1985; Moen et al., 2013). The effect of small-scale precipitation on scintillation has rarely been investigated. However, recent studies showed that ionospheric structures generating scintillation are highly localized, even smaller than the scale of an arc (Nishimura et al., 2023). Localized precipitation is closely related to density irregularities (Buschmann et al., 2023). Thus, it is important to test how much small-scale precipitation impacts scintillation. In this study, we explore the connections between a scintillation observation and the underlying plasma that produced it, specifically, the degree to which precipitation structures the auroral plasma and its effects on auroral scintillation. We employ the physics-based Geospace Environment Model of Ion-Neutral Interactions (GEMINI) (Zettergren & Semeter, 2012), coupled with the Satellite-beacon Ionospheric-scintillation Global Model of the upper Atmosphere (SIGMA) (K. Deshpande et al., 2014). By utilizing the SIGMA-GEMINI coupling (K. B. Deshpande & Zettergren, 2019), our research is able to investigate the specific role of electron precipitation in generating auroral scintillation.

2. Methodology

For an accurate depiction of signal propagation through electron-precipitated density structures, two models are essential: a high-resolution plasma model capable of capturing the density structures from an auroral arc at a high resolution (~100 m) and a propagation model that simulates the behavior of the signal as it traverses through these structures. To closely mimic the precipitation energies observed in realistic active auroral arcs, we incorporate precipitation spectral distributions similar to those inferred from, for example, all-sky imagers (ASI), narrow-field imagers, and PFISR. These tools are combined in this study in an effort to gain insights into how, in principle, these electron precipitation arcs generate density irregularities that may be responsible for auroral scintillation phenomena.

2.1. Modeling Tools: GEMINI-SIGMA

The GEMINI model is a three-dimensional ionospheric multifluid-electrodynamic model, first introduced by Zettergren and Semeter (2012), and further extended in subsequent studies (Zettergren & Snively, 2015; Zettergren et al., 2014). This model incorporates a fluid system of equations (Blelly & Schunk, 1993; Schunk & Sojka, 1997) that effectively describes the dynamics of the ionospheric plasma. The fluid system is self-consistently coupled to a quasi-electrodynamic treatment of auroral and neutral dynamo currents. Within the fluid system, the model includes mass, momentum, and energy conservation equations for various ionospheric species relevant to the E, F, and topside regions, including O^+ , NO^+ , N_2^+ , O_2^+ , N^+ , and H^+ . The conservation of mass equations accounts for chemical production and impact ionization (Fang et al., 2008), as well as chemical loss (Diloy et al., 1996; St.-Maurice & Laneville, 1998). Photoionization sources are determined using the methodology outlined in Solomon and Qian (2005), with solar fluxes obtained from the EUVAC model (Richards et al., 1994).

This study investigates the impacts of two key parameters, total energy flux (Q) and characteristic energy (E_0), on the phenomenon of scintillation. Within the GEMINI model, these density structures can be generated through various configurations by modifying factors such as precipitation flux, average energies, and the noise spectrum integrated into precipitation that induces small-scale disturbances. The spectrum of the small-scale features (\sim 500 m) within the arc structure derived from narrow-field camera data is used to constrain the modeling parameter space, such as spectral index (γ), arc width, and edge gradient scales.

SIGMA is a comprehensive three-dimensional electromagnetic wave propagation model that simulates signal transmission from a moving satellite to the ground through multiple phase screens. SIGMA proves particularly valuable in high-latitude regions, given its ability to account for the complex magnetic field line geometry in these areas. In the SIGMA model, the process starts with translating a spatial distribution of electron number density, obtained from either a spectral model for irregularities or a plasma model like GEMINI, into phase screens (Yeh & Liu, 1982). K. Deshpande et al. (2016) studied auroral and polar cap scintillation, where spectral models were used to create ionospheric structuring and an inverse method with SIGMA was employed to understand the physics of irregularities. We used the same technique in Vaggu et al. (2023) to study the morphology of auroral scintillation producing irregularities over Poker Flat. The physics-based model GEMINI was coupled with SIGMA to study scintillation in polar cap patches with gradient-drift instability as the underlying instability mechanism (K. B. Deshpande & Zettergren, 2019; Spicher et al., 2020). Once the phase screens are set up, the signal propagates through these multiple-phase screens toward the ground. To accurately represent the scattering,

VAGGU ET AL. 3 of 19

interference, reflection, and diffraction effects encountered during the signal propagation through this random medium, SIGMA employs a hybrid approach that combines the multiple-phase screens technique with a split-step solution to the forward propagation equation (C. Rino, 2011; C. L. Rino & Carrano, 2011). SIGMA produces several outputs, including a two-dimensional complex signal propagated on the ground and a high-rate scintillation phase and power time series sampled at 50 Hz. Parameters such as S4 and σ_{ϕ} , which characterize scintillation, can be readily extracted from these outputs.

Our approach involves a systematic modeling process using GEMINI to investigate the development of density structures in the E-region of the ionosphere due to the energetic electron precipitation. We consider various factors, including (a) the spatial and temporal characteristics of the aurora forms, (b) the total energy flux, and (c) the characteristic energy, all chosen to be representative of data from our example event. We vary these input parameters to gain a quantitative understanding of the direct influence of precipitation on the formation of ionospheric structures. We explore this parameter space based on characterizations derived from observed data, which includes camera images that provide information about the edge gradient scales, are motion, are width, and precipitation intensity in terms of both flux and energy in regions of scintillation, particularly in the vicinity of the auroras. The density observations obtained from PFISR offer insights into the altitudinal extent of density enhancements along the magnetic field lines. Considering that the scintillation measurements are taken by a satellite positioned at high elevation angles and oriented close to the magnetic field, the field-aligned beam density measurements from PFISR provide altitudinal density profiles closely aligned with the conditions favorable to scintillation activity.

We employ background conditions and small-scale precipitation (~500 m scales as observed by the narrow-field camera) to model the plasma density structures that are generated by electron precipitation. GEMINI-modeled precipitation density structures are imported into the SIGMA model like prior studies (K. B. Deshpande & Zettergren, 2019; Spicher et al., 2020; Lamarche et al., 2022) with the notable difference that the present focus is on the effects of precipitating electrons. Electron density structures are taken from the GEMINI simulation output files and rotated and interpolated in space and time onto the grid used internally in the SIGMA model. Within SIGMA, the radio wave emitted from the satellite is propagated through the electron-precipitated density structures (which are converted into a certain number of phase screens), allowing us to assess the effects of these simulated plasma density structures on the transmitted signal as it reaches the ground. SIGMA results for ground phase variations are then detrended to eliminate low-frequency effects, such as those arising from satellite motion.

The combined capabilities of GEMINI and SIGMA enable a coupled investigation into the relationship between precipitation-induced density structures and their influence on radio wave propagation, providing insights into the spatial and temporal effects of these density structures.

2.2. Imager and PFISR Data

To understand the variations in precipitation that lead to scintillation, it is crucial to establish the connection between the particle energy, precipitation flux, the resulting density structures, and the associated scintillation. This connection can be derived from the analysis of optical and radio data, particularly during conjunction events that involve simultaneous measurements using multiple instruments.

We chose for our analysis an auroral scintillation event occurring on 14 April 2013; both the University of Alaska's multispectral ASI and the Boston University's narrow field of view (FOV) camera at Poker Flat were operational at 08:54 (hh: mm) UTC, capturing data simultaneously, as shown in Figure 1. The ASI records all-sky images at 427.8 nm every 13 s. The narrow field camera operates at a 53 Hz sampling rate using the BG3 filter (Semeter et al., 2008), which is a wide-band filter that removes the long-lived oxygen metastable emission lines. The FOV covers a $\sim 20 \times 20$ km area when mapped to 110 km altitude near the magnetic zenith. The weather conditions were clear, providing optimal visibility for the observations. Both the ASI and narrow field camera detected a northwest-southeast oriented arc. The narrow field camera detected a discrete auroral arc displaying substructures, covering nearly the entire FOV, revealing fine-scale features within the auroral arc. The arc's visibility persisted for over 30 s, allowing for an extended observation period.

ASI optical measurements are utilized to assess background plasma inhomogeneities and their correlation with scintillation events. These help to characterize precipitation structures at sub-kilometer scales in the optical data, considering their spatial and temporal spectra within camera limitations, shown in Figure 1a. However, for

VAGGU ET AL. 4 of 19

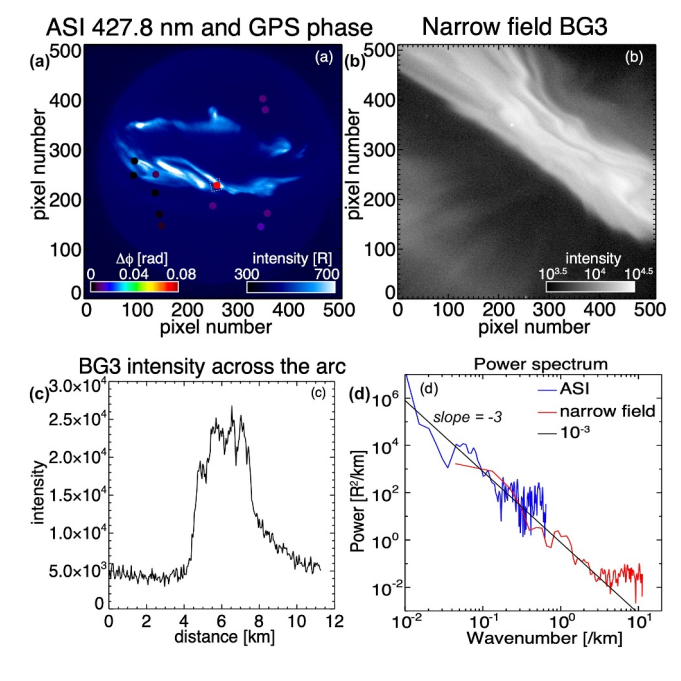


Figure 1. All-sky imagers (ASI) and narrow field imager data at Poker Flat at 08:54:34 UT on 14 April 2013. (a) ASI image at 427.8 nm. North is to the top, and east is to the right. The dashed square marks the field of view of the narrow-field imager. The colored dots indicate the variation of the Global Positioning System phase recorded by the POKR and CIGO receivers at Poker Flat and Fairbanks. (b) Narrow-field imager data. The intensity is in an arbitrary unit. North is to the top, and east is to the right. The star near pixels (225, 250) is Phecda in Ursa Major's constellation. (c) Line plot of the narrow-field imager intensity across the arc. The distance is measured from an arbitrary location to the west of the arc. (d) Power spectrum of the auroral intensity across the arc as a function of the wavenumber.

amplitude scintillation studies, it is important to examine structures at the Fresnel scale sizes, typically a few hundred meters. We extract small-scale precipitation statistics from the narrow-field camera data that provide insights to determine gradient scales, arc motion, arc width, and the internal structure of precipitation in terms of both flux and energy. It can be seen from Figure 1b that the arc exhibits a width of ~7 km, and the information of gradient scales referred from Figure 1c is used as a reference to model arc width and its edge gradient scales. Moreover, the spectrum of small-scale features across the arc structure derived from narrow field camera offer insights into scale sizes, typically in the range of a few hundred meters. From Figure 1d, the spectrum is approximated as a power law with a spectral slope of -3. This power law extends down to approximately a few hundred meters (about 500 m), while the flat spectrum at shorter wavelengths is considered to represent noise. We incorporate this spectrum into our model, introducing it to the energy flux at various precipitation intensities to examine the smallscale feature's impact on scintillation.

Additionally, we leverage PFISR E-region density measurements in conjunction with the scintillation data for a comprehensive characterization. In Figure 2, the geodetic Global Navigation Satellite System (GNSS) receiver at Poker Flat recorded phase and amplitude fluctuations during the observation, indicating the presence of scintillation effects caused by the interaction of the auroral arc with the ionospheric plasma. The GPS data collected from this GNSS receiver was obtained with a time resolution of 15 s, which may not be sufficient to capture detailed scintillation behavior. Nevertheless, the data proved useful in detecting low-frequency phase and amplitude fluctuations—phase fluctuations were observed between 08:53 and 08:57 UTC, followed by the detection of amplitude fluctuations at 08:57 UTC, as shown in Figures 2c and 2d. These fluctuations are associated with a transient TEC enhancement linked to the intensification of the auroral activity. We acknowledge that the TEC increase shown here could have considerable uncertainty. The GPS data exhibiting the high delta phase $(\delta\phi)$ value corre-

sponds to an elevation of approximately 75° (pseudo-random noise 29), signifying a notably elevated position in high-latitude regions. Moreover, its orientation is characterized by an angle of approximately 3° to the magnetic field, indicating an extremely close alignment. The field-aligned beam measurements obtained from PFISR reveal that the electron density reaches 1×10^{12} el/m³ at E-region altitudes, corresponding to the observed arc during the scintillation interval, as illustrated in Figure 2f. The PFISR density profile was used to estimate the energy flux and characteristic energy of precipitation (Nishimura et al., 2020). Here, the GLobal airglOW (GLOW) model (Solomon, 2017) was used for the forward modeling of the density from precipitation. The least squares method was used to find a combination of the energy flux and characteristic energy that minimizes the difference between the PFISR density and the GLOW density at each time. The MSIS model was used for the neutral atmosphere. The PFISR inversion suggests a peak potentially exceeding 100 mW/m^2 , though model calculations with GEMINI suggest that such a density can be generated with $\sim 50 \text{ mW/m}^2$. Additionally, using ASI observations, GLOW estimated a flux of approximately 7.5 mW/m^2 with an energy level of approximately 3 keV for the same observed arc.

There is a notable disparity between the camera-derived (\sim 7.5 mW/m²) and PFISR-derived (>100 mW/m²) energy fluxes for our event. One possible explanation is that the PFISR-estimated electron densities may well be contaminated by coherent scatter resulting from beam-induced Langmuir turbulence, which can lead to an overestimate in electron density. However, there is no conclusive evidence of Langmuir turbulence observed in the PFISR data. Due to the absence of any certain ways of resolving these differences, we have chosen to run our simulation with a range of energy fluxes commensurate with various estimates from this event. Specifically, our data for this event can only be bound by the total energy flux as being in the range 5–50 mW/m²; hence, several different simulation cases are required to understand the potential impacts of these flux levels on scintillation.

VAGGU ET AL. 5 of 19

Wiley Online Library on [03/09/2024]. See the Terms and Condition

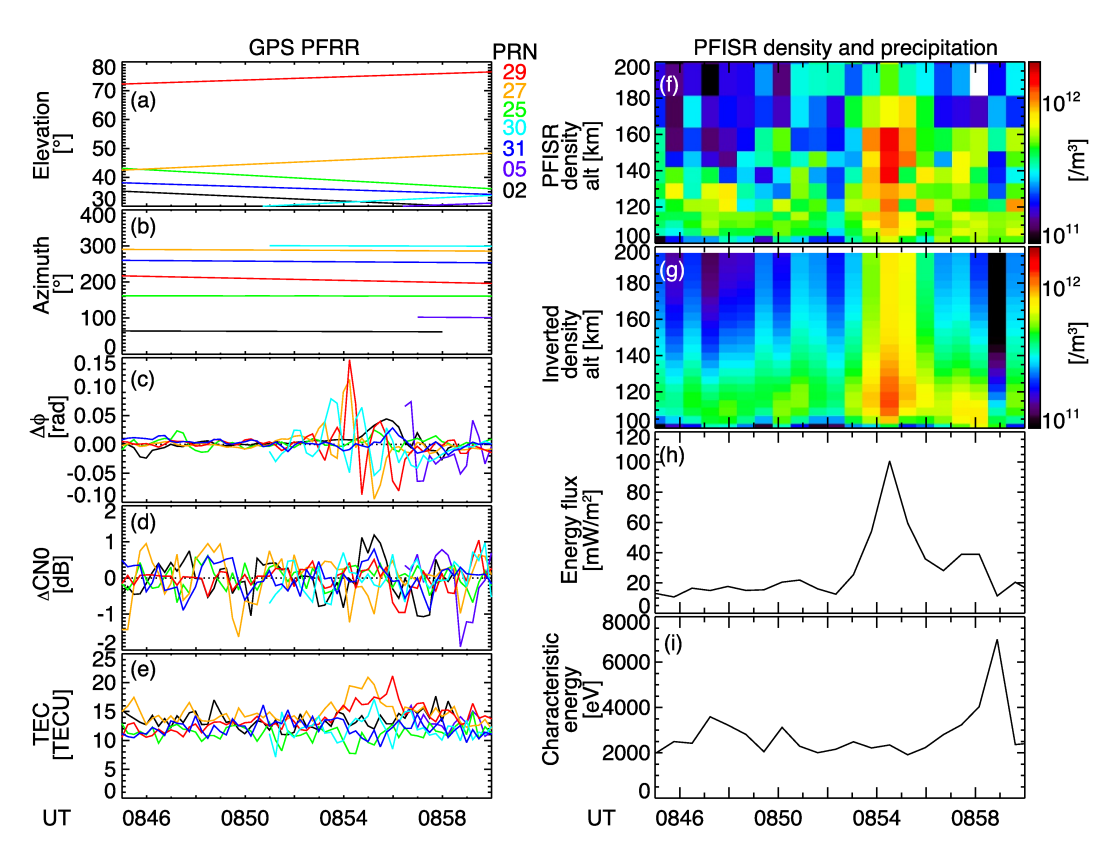


Figure 2. (left) Global Positioning System receiver data at PFRR. The panels shown are (a) Elevation angle, (b) azimuth angle, (c) phase variations, (d) Carrier-to-noise ratio variations, and (e) total electron content. The data are color-coded by the pseudo-random noise code. (right) Poker Flat Incoherent Scatter Radar (PFISR) and precipitation parameters. The panels shown are (f) PFISR density along the field-aligned beam (beam 13), (g) density along the beam fitted using the GLobal airglOW Model model, (h) energy flux that is used for panel (g), and (i) characteristic energy that is used for panel (g).

2.3. Modeling Approach

The intent of this work is to study the hypothetical dependence of irregularity formation and attendant scintillation on the character of the precipitating electrons. Data shown in Figures 1 and 2 are used as guidance and motivation for constructing these hypothetical cases where we focus on the potential roles of several parameters in producing scintillation, namely the motion of the arc, the total energy flux in the arc, and the spectrum of small-scale structures within the arc.

2.3.1. Synthesis of Auroral Features in GEMINI-SIGMA

For all simulations in this study, the *mesoscale* arc feature used is deterministic, with parameters chosen to mimic the camera data summarized in Figure 1:

$$Q_{shape}(x, y, t) = \exp\left(\frac{-(x - v_x t)^8}{2\sigma_x^8}\right) \exp\left(\frac{-(y - y_0(x) - v_y t)^8}{2\sigma_y^8}\right)$$
(1)

where the arc widths $\sigma_{x,y}$ are chosen to be fixed quantities for this study to generate a feature roughly the size of the arc as it appears in the narrowfield data. The parameter y_0 is chosen to give the arc some amount of curvature, while the arc motion is determined by varying the $v_{x,y}$ parameters in some of our calculations (see results section below).

Small-scale structures are captured in our modeling via the inclusion of a noise-like spectrum of fluctuations in the total energy flux. This spectrum is imposed within the larger scale, deterministic structure (Equation 1) to mimic the overall mesoscale shape function of the auroral arc. We use a power spectrum, P_{QQ} (units of $1/m^6$ Hz²), based

VAGGU ET AL. 6 of 19

on a power law like our event of interest (though we choose various different parameters for spectral index). The spectrum chosen for our work is characterized by two outer scales $\ell_{x,y}$:

$$P_{QQ}(k_x, k_y) = P_0 \left(\left(\frac{k_x}{2\pi \ell_x^{-1}} \right)^2 + \left(\frac{k_y}{2\pi \ell_y^{-1}} \right)^2 \right)^{\gamma/2} \qquad \left(\frac{k_x}{2\pi \ell_x^{-1}} \right)^2 + \left(\frac{k_y}{2\pi \ell_y^{-1}} \right)^2 > 1$$

$$= P_0 \qquad \text{otherwise}$$
(2)

where γ is the spectral index, and the spatial scales are defined to mimic the fact that we typically see differentsized internal structures in the direction along versus across the arc (e.g., Figure 1). In our work, we choose the wavenumbers $k_{x,y}$ associated with scale lengths $\ell_{x,y}$ of 2 and 20 km in x- and y-directions, respectively.

A specific realization of total energy flux is obtained by converting power spectral density in signal amplitude and then applying a random phase and taking the inverse Fourier Transform (numerically applied as an inverse Fast Fourier Transform)—taking care to observe signal symmetry considerations in the generation of the random phase so that the results is purely real-valued. The realizations remain fixed throughout the simulation, creating a consistent representation of static precipitation. This configuration allows us to investigate the influence of constant noise realizations and make the time variability in the noise spectrum a primary focus for future research.

$$Q_{small}(x, y) = \frac{1}{(2\pi)^2} \int_{-\infty}^{\infty} \int_{-\infty}^{\infty} \left(\sqrt{P_{QQ}(k_x, k_y)} e^{i2\pi a(x, y)} \right) e^{ik_x x} e^{ik_y y} dk_x dk_y$$
 (3)

where a(x, y) is a uniformly distributed field of random numbers between 0 and 1. Of course, in practice, all quantities and operations are discretized on some mesh used for input data but shown here in continuous form for simplicity. Finally, the full input for GEMINI-SIGMA is constructed as follows:

$$Q = Q_{shape}Q_0(1 + \alpha Q_{small}) \tag{4}$$

The small-scale precipitation in this study effectively held constant with time, while the arc envelope itself varied slowly in some of the simulations presented in the Results section. α is an adjustable fraction to control relative noise levels; in this work, we use $\alpha = 1$, meaning the noise amplitude is equal to the peak intensity of total energy flux (Q_0) .

2.3.2. Summary of Processing Approach

In this study, we have employed a highly non-uniform grid within GEMINI, adjusting the resolution to achieve approximately 100 m grid spacing at the center-most part of the grid. This approach allows us to capture detailed spatial and temporal variations in the density structures within the ionosphere. The values of total energy flux for the modeling are taken from ASI and PFISR observations, as detailed in the previous section. To account for smaller-scale fluctuations, we incorporate a spectrum of ionospheric turbulence that follows a power-law behavior with a spectral index (γ) of -3, consistent with the observed data. This representation enables us to effectively capture the short-wavelength features of electron density irregularities, which are crucial in generating scintillations. Within the GEMINI model, we derive impact ionization rates, providing valuable insights into the altitudinal profiles of plasma density, electron and ion temperatures, and other relevant parameters. These profiles are strongly influenced by the intensity of electron energy depositions (Q and E_0).

Figure 3 presents the comprehensive simulation process. This process involves creating the GEMINI grid structure, which is utilized as the foundational framework to incorporate model inputs for generating plasma parameter profiles determined by the GEMINI chemistry. We further import the density structures modeled in GEMINI, resulting from electron precipitation, into SIGMA. Within SIGMA, we simulate and extract the scintillation effects produced by precipitated density structures. For the present study, we have constructed simulation inputs using a number of different combinations of the input parameters of interest, presented in Table 1.

VAGGU ET AL. 7 of 19

21699402, 2024, 7, Downloaded from https://agupubs.onlinelibrary.wiley.com/doi/10.1029/2024/A032443 by Yukitoshi Nishimura - Boston University , Wiley Online Library on [03/09/2024]. See the Terms and Condition

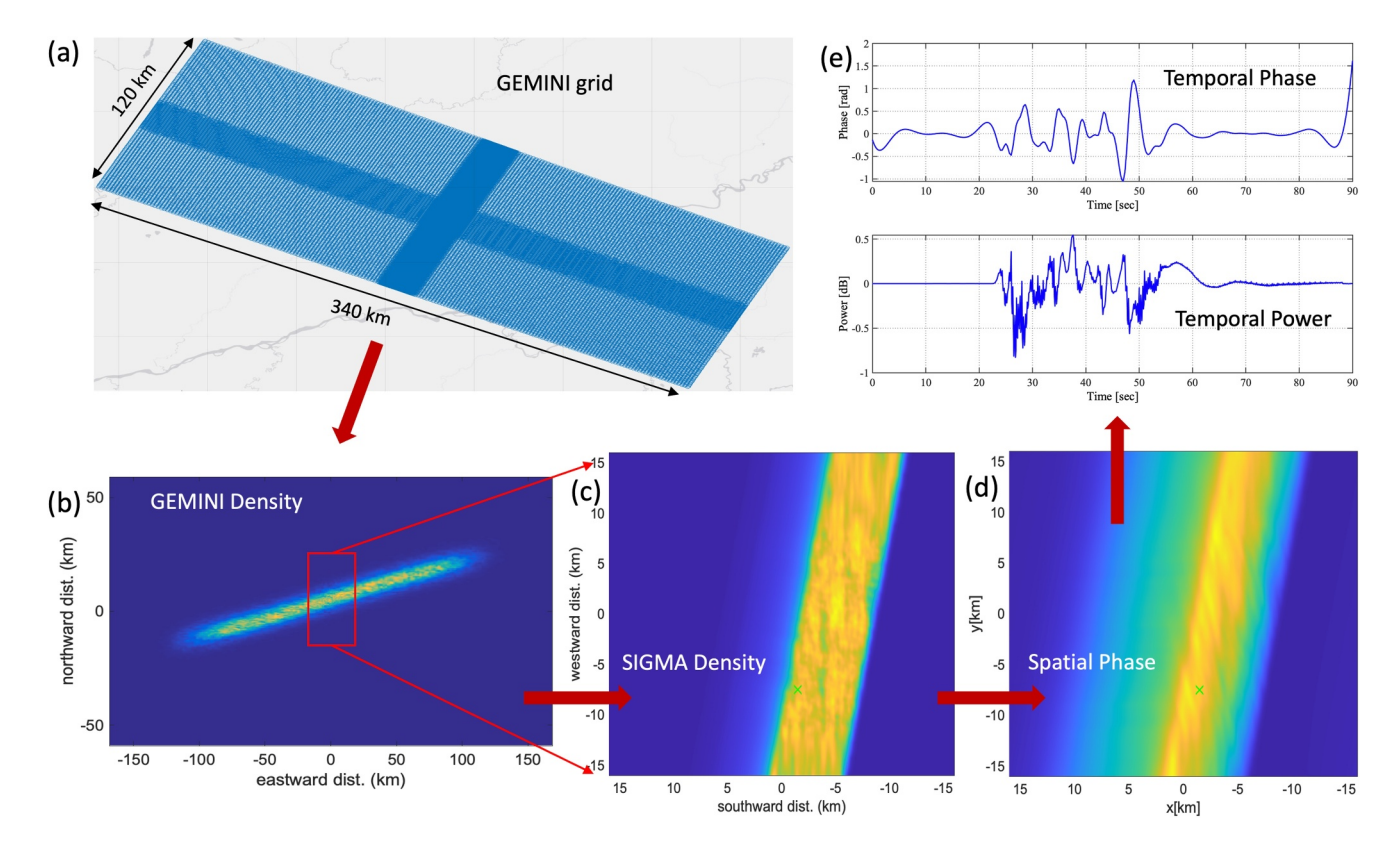


Figure 3. The sequence (a) through (e) depicts the entire simulation process, starting from generating a non-uniform high-resolution GEMINI grid, as shown in (a). This grid is employed to generate plasma parameter profiles, such as the density profile visualized in (b). The density profile modeled in GEMINI is imported into Satellite-beacon Ionospheric-scintillation Global Model of the upper Atmosphere and showcased as (c). In the next step, the spatial fluctuations of the propagated signal are captured on the ground, for example, the simulated spatial phase in (d). Finally, the detrended temporal signal fluctuations are extracted from these spatial fluctuations, for example, the detrended phase shown in (e).

3. Results

This section provides an overview of the results from the set of model simulations summarized in Table 1 (with some minor additions left to supplementary materials)—this set encapsulates a range of total energy fluxes implied by the data for our example event and also different commonly observed drifts and spectral indices.

3.1. Effect of Precipitating Total Energy Flux on Scintillation

By examining the impact of increased energy flux on the scintillation, our findings reveal a direct correlation between precipitation energy flux and scintillation intensity. As outlined in Section 2.2, we have established an energy flux of 50 mW/m² as a value at least somewhat consistent with generating the electron densities illustrated in Figure 2. Despite the GLOW estimate indicating a flux exceeding 100 mW/m², we opted to utilize a flux of 50 mW/m² which generated the density intensities that align with the PFISR densities, to evaluate the effects of energy flux on scintillation. Additionally, we have chosen a value of 25 mW/m² for relatively weaker arcs. As the

Table 1List of Simulations and the Choices of the Parameters to Analyze the Effects of Precipitation, Spectral Index, and Drift Velocity on Scintillation

Case	SI	Flux (mW/m ²)	Energy (keV)	Drift speed (m/s)	Drift direction ^a	H _{iono} (km)
Section 3.1	$\gamma = -5/3$	25 versus 50	2	300	180°	110
Section 3.2	$\gamma = -5/3$ versus $\gamma = -3$	50	2	300	180°	110
Section 3.3	$\gamma = -3$	50	2	300 versus 600	180°	110

^aDirection counter-clockwise from geomagnetic south.

VAGGU ET AL. 8 of 19

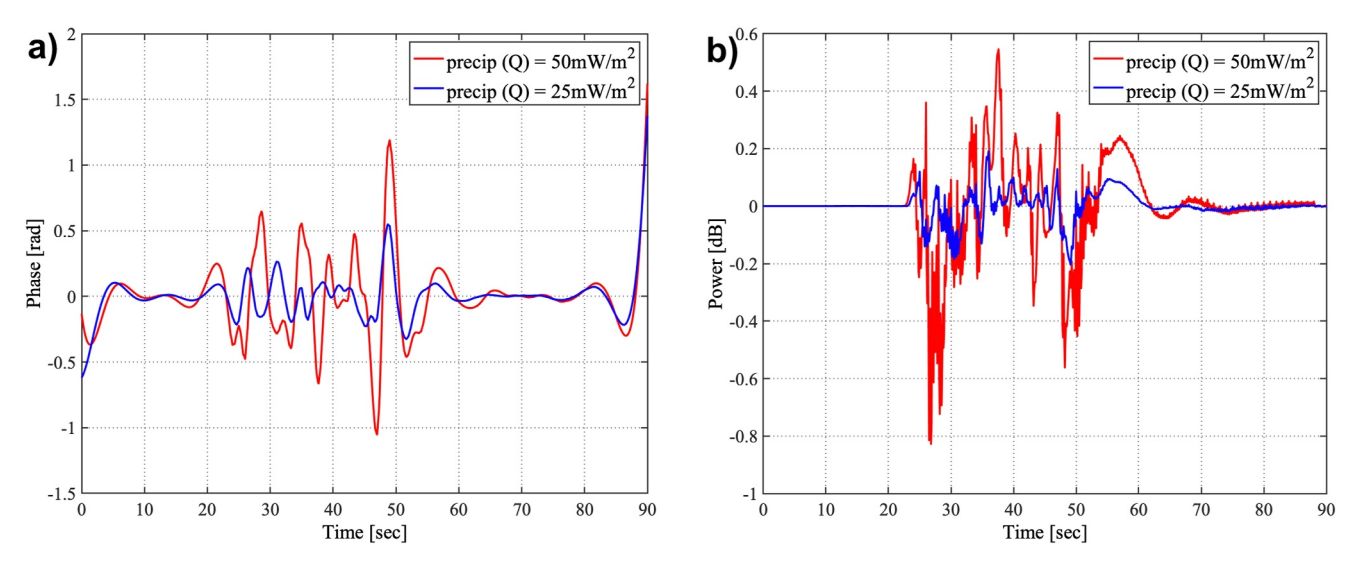


Figure 4. Satellite-beacon Ionospheric-scintillation Global Model of the upper Atmosphere simulated signal fluctuations in (a) phase and (b) power for two different precipitation energy flux levels.

energy flux increases from $Q=25~\text{mW/m}^2$ to $Q=50~\text{mW/m}^2$, the electron density in the E-region also rises significantly from approximately $6.5\times10^{11}~\text{el/m}^3$, reaching $1\times10^{12}~\text{el/m}^3$, respectively. This elevated electron density becomes a source of scintillation at E-region altitudes. Importantly, comparisons made under the same power law noise spectrum ($\gamma=-5/3$) and arc speeds ($v_y=300~\text{m/s}$) demonstrate that higher energy flux levels result in stronger scintillation, as seen in Figure 4. In the case of $Q=50~\text{mW/m}^2$, fluctuations in signal phase exceeded 2 rad peak to peak (P2P), with power fluctuations of approximately 1.4 dB P2P, surpassing scintillation intensities observed for $Q=25~\text{mW/m}^2$. Thus, it is evident that higher energy fluxes lead to higher electron densities, consequently causing more pronounced scintillation effects. On the contrary, we also analyzed the minimum energy flux thresholds necessary to induce phase and amplitude fluctuations by systematically decreasing the energy fluxes to determine the lower energy limit that triggers scintillation effects. Through our analysis, it is revealed that a minimum energy flux of approximately 7.5 mW/m² ($Q_0=5$, $\alpha=0.33$) is required for detectable phase scintillation, resulting in a density of $3.5\times10^{11}~\text{el/m}^3$, which produces phase fluctuations of 0.4 rad P2P and power fluctuations of 0.1 dB P2P (figure shown as supplementary). This level of energy flux is notably close to that suggested by analysis of the optical data ($\sim7.5~\text{mW/m}^2$).

3.2. Effect of Spectral Index on Scintillation

As mentioned previously, we introduce an ionospheric turbulence noise spectrum to the precipitation that follows a power-law behavior with a spectral slope of -3, consistent with observed data to account for the stochastic nature of electron density. This modeling approach allows us to effectively capture the finer-scale variations in electron density irregularities, which are important for scintillation generation. Initially, we adopted the Kolmogorov turbulence spectrum to describe energy distribution across various scales, including outer and inner scales, with a spectral slope of -5/3. However, to maintain consistency with auroral observations, we have also incorporated a spectral slope of -3, shown in Figure 1d. In the previous example, we observed the influence of increased energy flux on scintillation intensities when introducing a noise spectrum characterized by a slope of -5/3. An intriguing observation emerged when we altered the noise spectrum to slope = -3. Specifically, when the noise spectral slope changed to -3, and the arc velocity remained at 300 m/s, fluctuations in signal phase decreased from 2 rad P2P (observed with slope = -5/3) to 1 rad P2P, shown in Figure 5. This suggests that the turbulent noise spectrum responsible for inducing small-scale density irregularities within precipitation plays a crucial role in radio signal propagation. A steeper slope in the noise spectrum results in reduced scintillation effects. Furthermore, this reduction in scintillation intensity is also observed in power fluctuations when transitioning from a noise spectrum with slope = -5/3 to slope = -3. A noise spectrum characterized by a spectral slope of -3 generates a steeper profile with fewer short-wavelength features. Consequently, this leads to fewer scintillation-scale-sized structures, thus having a reduced impact on scintillation activity. We note that modifying

VAGGU ET AL. 9 of 19

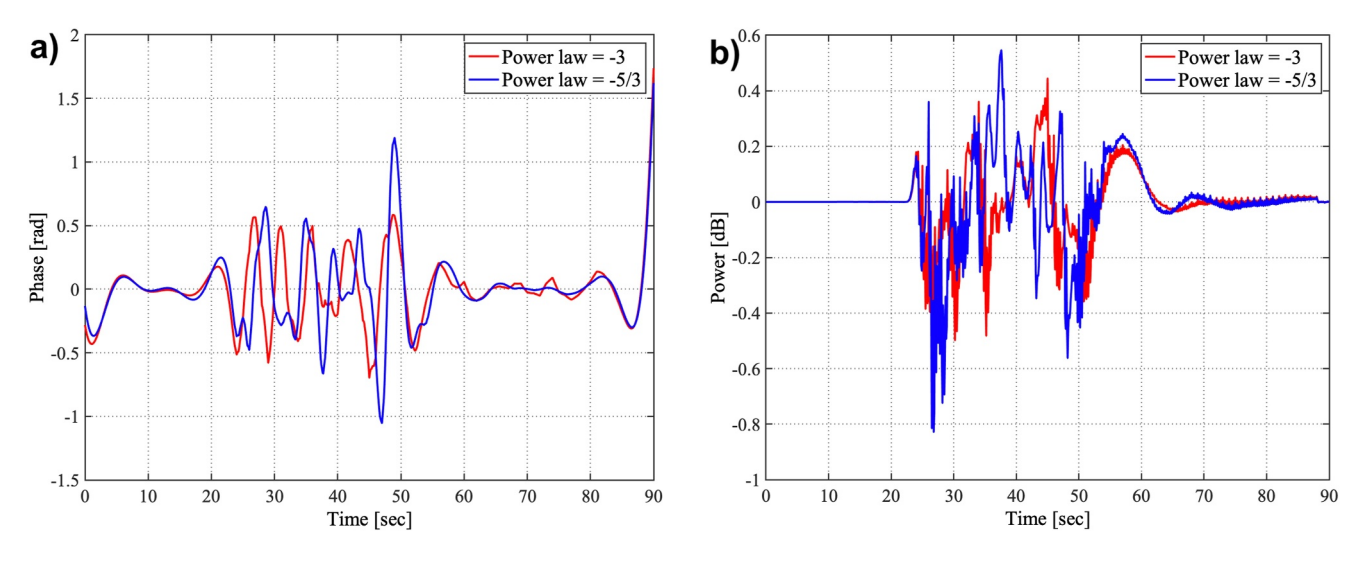


Figure 5. Variation in the intensity of (a) signal phase fluctuations and (b) signal power fluctuations as the noise spectrum varies.

the spectral index results in an alteration of the total power within the fluctuating component (i.e., the integral over k). However, for a steeper spectral index ($\gamma = -3$), the power is concentrated more at lower frequencies (longer wavelengths), while a flatter spectral index ($\gamma = -5/3$) is distributed across both longer and shorter wavelengths. Altering the spectrum in this manner preserved the power at the outer scale, which we deemed desirable for this study since those scales are fairly well-constrained by the data. Therefore, introducing a flatter spectrum creates more structures at the scintillation scales, causing a stronger scintillation activity. In the discussion section, we explore how long- and short-wavelength features distinctly influence the signal phase and power.

3.3. Effect of Across-Arc (North-South) Motion on Scintillation

In addition to precipitation energy flux and the turbulent spectrum, are velocity is an important factor influencing scintillation intensity. Notably, when the noise spectrum is adjusted to a slope of -3 with an arc velocity (v_y) of 300 m/s, scintillation intensity remains relatively lower, even in the presence of higher energy fluxes. To evaluate the impact of arc velocities on signal scintillation, we conducted a detailed analysis including two distinct arc velocities: 300 and 600 m/s. This investigation was conducted while maintaining a noise spectrum with a slope of -3 and a constant energy flux of 50 mW/m². Interestingly, our analysis reveals that scintillation intensity

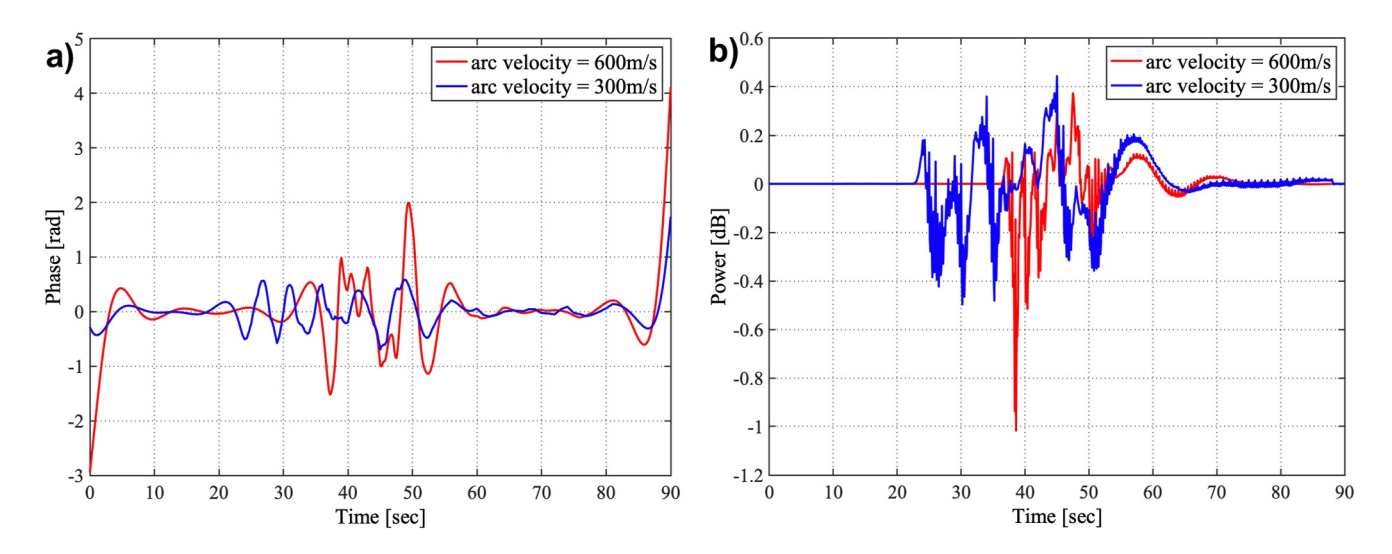


Figure 6. Effects of arc velocities on (a) signal phase and (b) signal power as the signal propagates through the density structures with two different velocities.

VAGGU ET AL. 10 of 19

wiley.com/doi/10.1029/2024JA032443 by Yukitoshi Nishimura

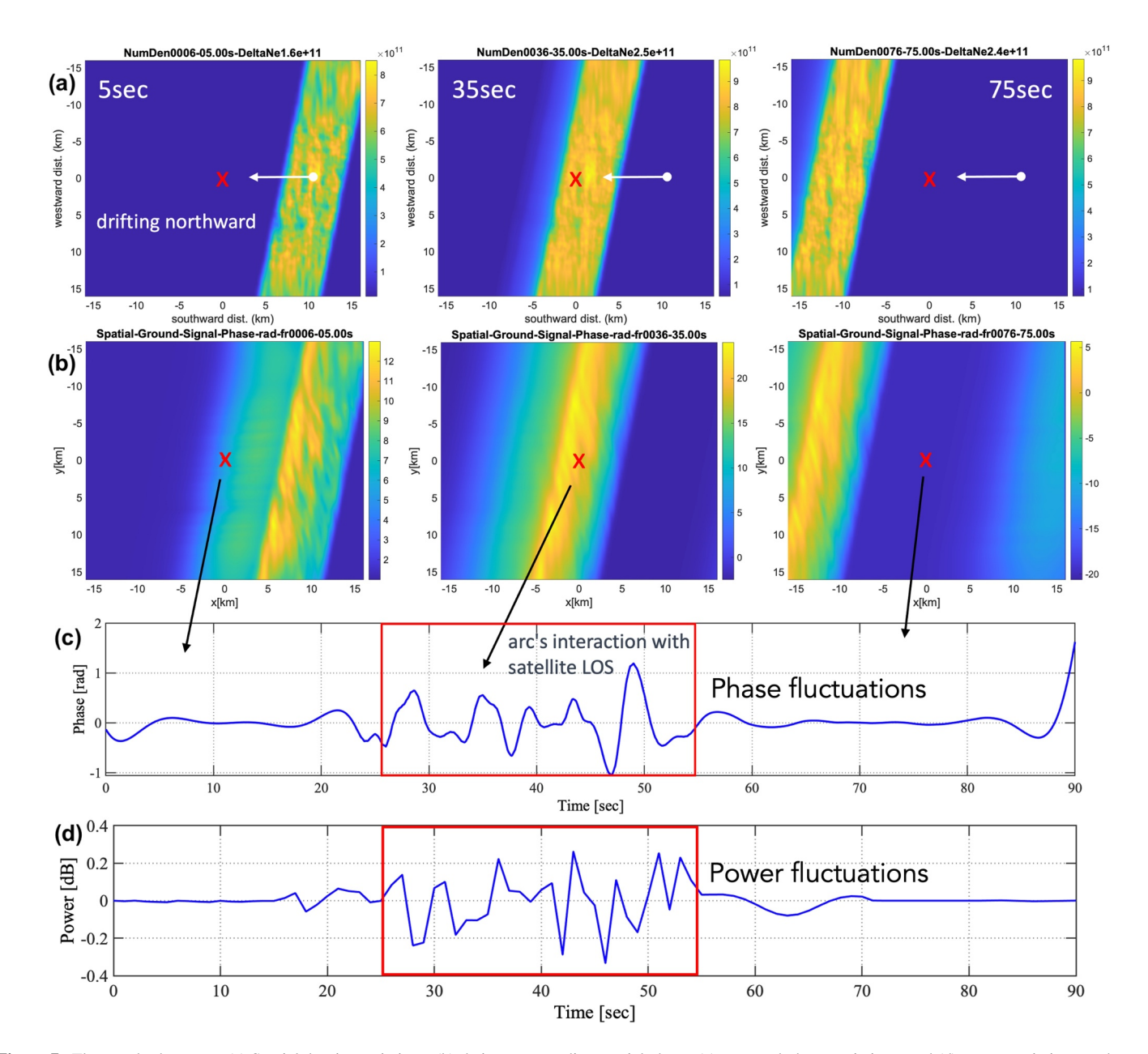


Figure 7. The panels shown are (a) Spatial density variations, (b) their corresponding spatial phase, (c) temporal phase variations, and (d) power variations as the *arc drifts across the satellite LOS*. Density units are el/m³, and ground phase units are radians.

amplifies as the arc velocity increases from 300 to 600 m/s, as represented in Figure 6. This shows higher arc velocities are associated with more noticeable and pronounced scintillation effects.

Remnant ionization is left in the wake of the arc as it moves (Figure 7); this is due to the plasma chemical lifetime in the E-region, which is of the order of a few seconds. The arc structure itself acts as a refractive medium, inducing refractive effects on the transmitted signal, predominantly causing phase fluctuations. As the arc velocity increases, these refractive effects intensify, notably enhancing the phase scintillation activity. The line-of-sight (LOS) interaction with the arc occurs at a later instance in the 600 m/s case (utilizing a larger grid space), resulting in signal fluctuations being detected later compared to the 300 m/s case.

To investigate the impact of the combination of satellite LOS and precipitation density structures on scintillations, we analyze signal phase fluctuations observed at the ground level as the arc structure interacts with LOS. Figure 7 is an example showcasing the precipitation density structures and their effects on signal propagation as the

VAGGU ET AL.

wiley.com/doi/10.1029/2024JA032443 by Yukitoshi Nishimura

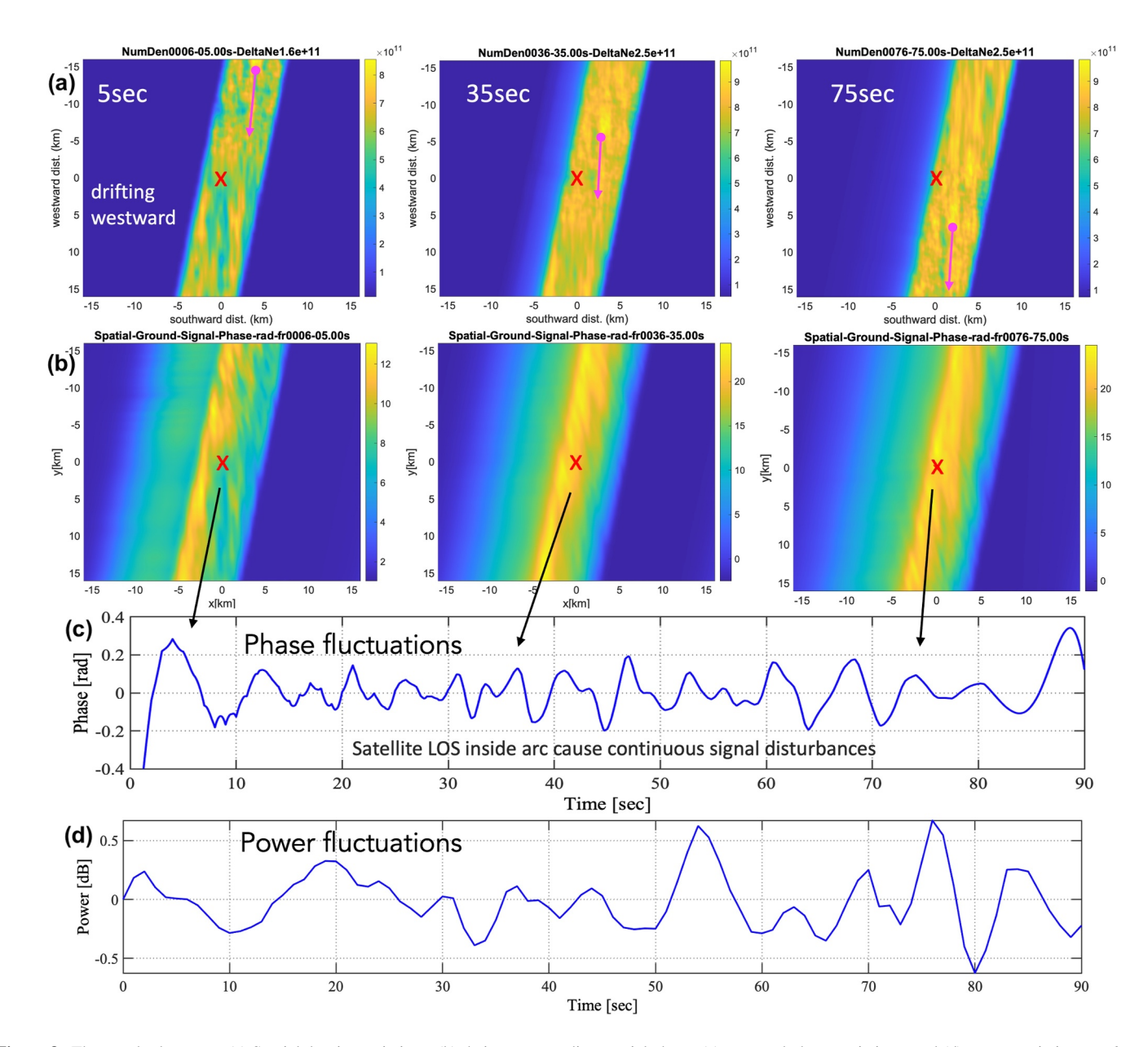


Figure 8. The panels shown are (a) Spatial density variations, (b) their corresponding spatial phase, (c) temporal phase variations, and (d) power variations as *the arc moves along the satellite LOS*. Density units are el/m³, and ground phase units are radians.

structure moves across the LOS. The top panels of the figure depict the arc structures at three time stamps during the simulation, spanning from the initial time (left) to the end of the simulation (right). The arc gradually moves northward during the simulation and intersects with the LOS between 25 and 55 s. This northward motion continues until the simulation ends at 90 s. We continuously monitor signal disruptions during the simulation, and notable phase fluctuations are evident when LOS intersects density structures of scale sizes that are sensitive to scintillation, as shown in Figure 7. The intensity of the scintillation varies with precipitation strength, scale sizes within the precipitation, and its drift speed, as discussed in previous sections. Weak structures may not impact the satellite signal, while strong ones induce stronger scintillation activity.

3.4. Effect of Along-Arc Motion on Scintillation

In contrast with Figures 7 and 8 illustrates the scintillation effects as the arc structure drifts *along* the LOS. Unlike the previous case, the satellite LOS consistently remains close to the arc. Consequently, a heightened interaction

VAGGU ET AL. 12 of 19

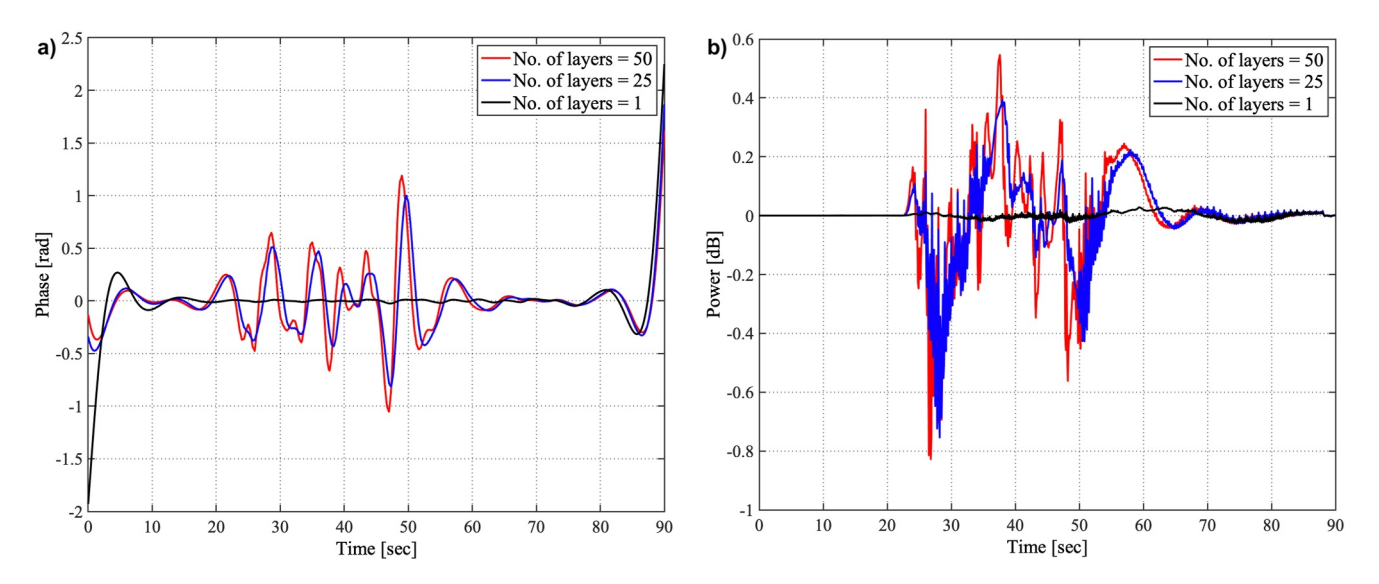


Figure 9. Fluctuations in (a) signal phase and (b) signal power as the number of irregularity layers increases.

between the LOS and the arc results in a more pronounced impact of the auroral arc and continuous signal disturbances. These disturbances become apparent in the received signal on the ground, shown in Figure 8. As mentioned earlier, the intensity of the scintillation varies with precipitation strength, scale sizes within the precipitation, and drift speed. In GEMINI, we resolve an outer scale in the north-south direction, constrained by the width of the arc (approximately 7 km in this case), and inner scales are resolved to 100 m, occasionally extending below this threshold. The broad scales are influenced by the width of the arc, giving rise to phase fluctuations, while the smaller scales could contribute to amplitude fluctuations. In both cases, stronger scintillation effects are observed when the LOS intersects the edges of the arc structure. Utilizing edge gradient scales extracted from the narrow field camera data, we are able to mimic structures resembling the active auroral arcs at the edges of the arc. These edge gradient scale structures appear to have a more pronounced influence on the signal as it traverses through them.

3.5. Irregularity Layer and Scintillation

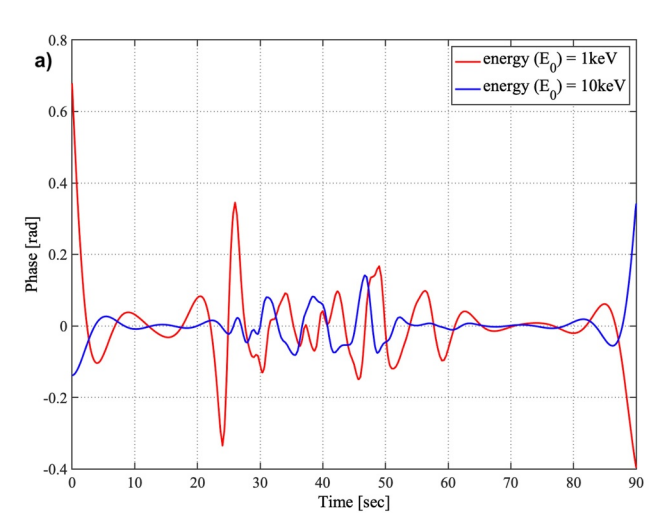
In the SIGMA model, we simulate the three-dimensional propagation of a satellite signal as it approaches the irregularity at an oblique angle and passes through it. This irregularity is represented as an arrangement of diffractive phase screens or irregularity layers. According to Yeh and Liu (1982), the term "phase screen" represents an assumption where each layer is thin enough to introduce random phase perturbations into the incident signal. These perturbations are directly proportionate to the electron content within that specific layer. However, it's crucial to note that the signal's amplitude remains constant inside the layer. As the wave propagates in free space between two layers, perturbations in the amplitude may start to develop. Here, the density structures produced by electron precipitation, as simulated within GEMINI, are given as input to SIGMA, where we divide the density into the number of layers representing the phase screens. The impact of varying numbers of irregularity layers on signal propagation within SIGMA is shown in Figure 9. It is noticeable that an increase in the number of irregularity layers tends to enhance scintillation activity. The increase in the number of irregularity layers intensifies signal fluctuations through a compounded effect arising from disruptions caused by these irregularities. As the signal traverses through multiple layers with varying electron density, these disruptions amplify due to the interference at each layer, contributing significantly to signal fluctuations.

4. Discussion

4.1. Phase Fluctuation Detectability Versus Total Energy Flux

The total energy flux parameter is most closely connected with the ionization rate (roughly proportional), and hence plasma density increases. Results presented in this study suggest that the types of phase scintillations seen in our example event are associated with 25–50 mW/m² precipitation for our chosen energy of 2 keV. At a

VAGGU ET AL. 13 of 19



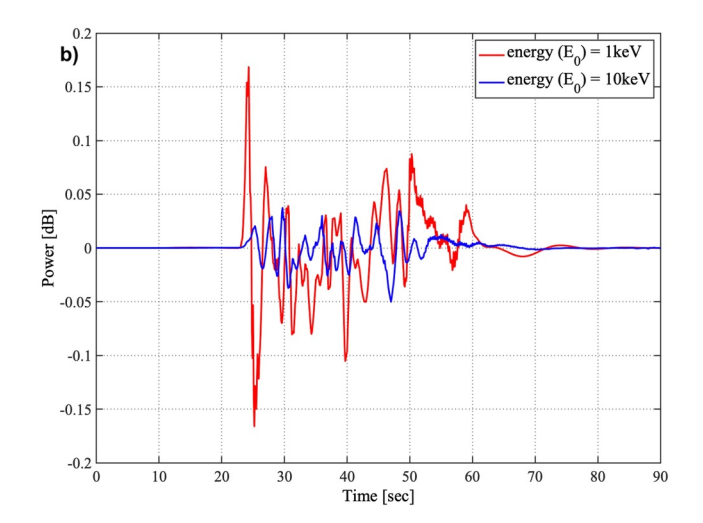


Figure 10. The simulated signal fluctuations in (a) phase and (b) power were analyzed for different precipitation energy levels.

relatively low incoming flux (\sim 7.5 mW/m²), we observe a weaker phase scintillation activity; this level of energy flux is probably near the minimum threshold for generating such detectable activity. The amount of phase scintillation present in our model increases very roughly in proportion to the total energy flux overall (Figure 4 and supplementary materials). Notably, amplitude scintillation remains quite small for all of the simulations presented in this work.

4.2. Effect of Characteristic Energy on Scintillation

In our analysis of the influence of precipitation energy on scintillation phenomena, we compared the scintillation effects induced by precipitation energies of 1 and 10 keV, shown in Figure 10. The total energy flux was maintained at $\sim 10 \text{ mW/m}^2$, which generated a density peak ranging from 4 to $5 \times 10^{11} \text{ el/m}^3$ for both the cases. It is noticed that high-energy precipitation (10 keV) produced the peak electron densities occurring at below 100 km altitudes, whereas the low-energy precipitation (1 keV) produced the peak densities at around 140 km altitudes (density profiles are added as supplementary material). It is also observed that the thickness of the plasma layer generated by high-energy precipitation exhibits a thinner profile (approximately less than 10 km) compared to the plasma layer thickness ($\sim 100 \text{ km}$) generated by low-energy precipitation. For 1 keV energy with a plasma layer thickness of $\sim 100 \text{ km}$, the intensity of the scintillation is relatively stronger when compared to the 10 keV energy case, shown in Figure 10. These variations in plasma layer thickness at different energies did notably affect the intensity of phase and power fluctuations. Unlike the variations in total energy flux, which showed a substantial impact on fluctuations, the characteristic energy itself does not significantly influence signal fluctuations.

4.3. Scintillation Associated With Higher Energy Fluxes

The energy fluxes used for this study are based on the PFISR density-derived fluxes using the GLOW model, suggesting a peak exceeding 100 mW/m^2 . However, scintillation data available for this event has a 15-s time resolution, limiting our ability to analyze the high-rate scintillation behavior. We identified another relevant event occurring on 12 March 2015 over Poker Flat. During this event, high-rate (100 Hz) scintillation data was captured by SAGA, associated with higher energy flux recordings from ASI and density measurements from PFISR, shown in Figure 11. The ASI recorded energy fluxes peaking above 100 mW/m^2 with PFISR observed densities ranging between 5 and $6 \times 10^{11} \text{ el/m}^3$. These measurements are correlated with SAGA-observed high-rate phase and power fluctuations. It suggests that the energy fluxes used in our simulations ($25-50 \text{ mW/m}^2$) fall within ranges observable by ASI, and the simulated high-rate scintillation intensities are at comparable levels with the ones observed by SAGA over Poker Flat.

4.4. Effects of Model Resolution on Diffraction (Amplitude Scintillation)

All simulations presented to this point have been conducted with 100 m grid resolution in the SIGMA analysis region of the GEMINI mesh. This section explores, briefly, the role of resolution and noise-like structure in our

VAGGU ET AL. 14 of 19

, Wiley Online Library on [03/09/2024]. See

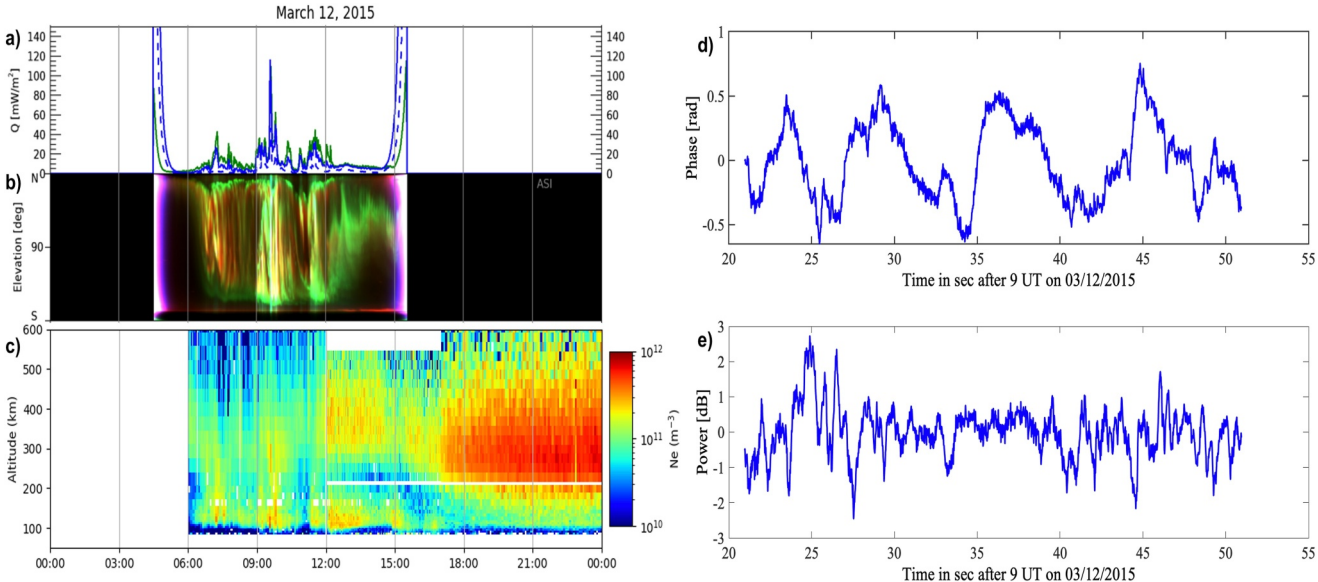


Figure 11. All-sky imagers (ASI), Poker Flat Incoherent Scatter Radar (PFISR), and Scintillation Auroral GPS Array observations during the event on 12 March 2015 over Poker Flat. (a) Energy flux derived from ASI, (b) ASI observations depicting the auroral emissions, (c) PFISR density measurements, (d) and (e) Scintillation Auroral GPS Array-measured high-rate phase and power fluctuations, respectively.

models on amplitude scintillation for cases similar to what has been presented above. To this end, we have conducted comparisons of our simulations at 100 m and 1 km resolution using different noise amplitudes (set by our parameter α in Equation 4). Figure 12 shows the results of this additional analysis. All results in Figure 12 are conducted using a flux of ~7.5 mW/m² (lower energy bound), thus the weaker scintillation intensity.

For our test simulations on a 1 km grid, the basic arc structure, without noise, acts as a purely refractive medium that induces phase variations without affecting signal power (Figures 12c and 12d). These variations originate from structures spanning scales between 1 km (grid resolution) and approximately 7 km (arc width/outer scale)—which excludes the structures of small-scale precipitation at sizes below 1 km. The enhancement in phase variations correlates with an increase in noise amplitude, emphasizing the influence of the long-wavelength regime (1 to \sim 7 km) of the power law noise spectrum on generating phase variations.

The transition from a 1 km grid to a 100 m grid presents a distinct scenario. The finer 100 m grid resolution allows us to create Fresnel scale structures using the power law noise spectrum, which is crucial for amplitude scintillation. As previously mentioned, the arc itself (without noise) functions as a refractive medium generating phase variation. It is worth noting that, even over a 100 m grid, virtually no amplitude scintillation activity (black line in Figure 12b) is observed as the basic arc structure (without noise) lacks small-scale structures that cause diffractive changes in signal power. The addition of progressively higher levels of small-scale precipitation structure amplifies both phase and amplitude scintillation activity (Figures 12a and 12b). The long wavelength features within the noise spectrum continue to contribute to phase fluctuations, while the shorter wavelength features within the spectrum contribute to power fluctuations. These shorter wavelength features, ranging from less than 1 km to \sim 100 m, contribute to generating Fresnel scale features, which become important in causing amplitude scintillation.

Comparisons shown in Figure 12 show that the overall arc mesoscale structure acts solely as a refractive medium, predominantly inducing phase variations. However, integrating the power law noise spectrum alongside a grid resolution capable of resolving small-scale structures facilitates contributions to both phase (from the long-wavelength regime) and power (from the short-wavelength regime) variations. Our observations underscore the significance of structures larger than 1 km for generating phase variations and those smaller than 1 km for generating power variations and indicate that the latter, while seldom resolved except in narrow-field camera data acquired very near magnetic zenith (Dahlgren et al., 2013), appear to be required to study amplitude scintillation.

VAGGU ET AL. 15 of 19

- Boston University, Wiley Online Library on [03/09/2024]. See the Terms

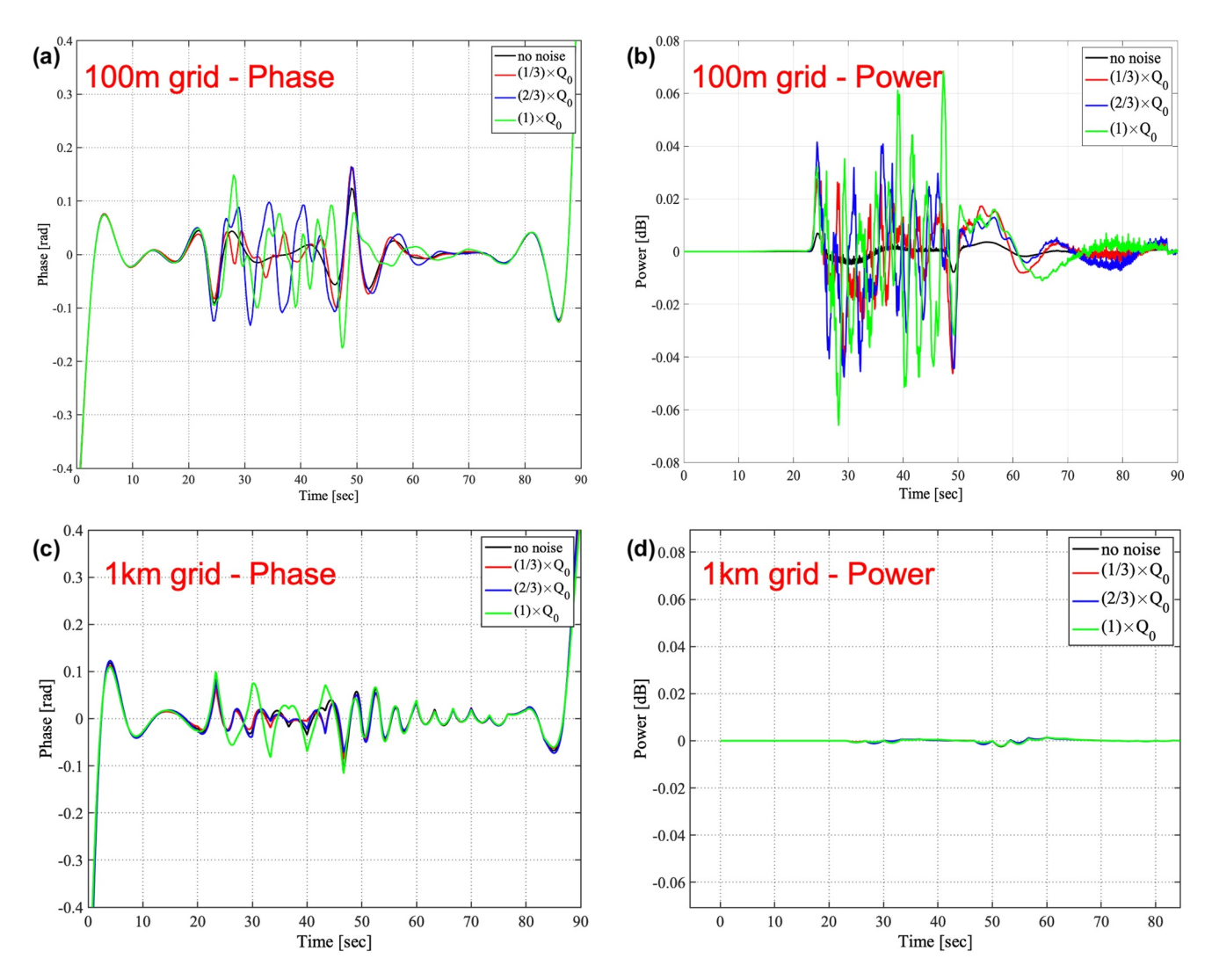


Figure 12. Illustrating the influence of 100 m grid (small-scale precipitation) versus 1 km grid (large-scale precipitation). The amplitude scintillation triggers when a noise spectrum that includes small-scale features is introduced. The noise realizations impact both phase and amplitude. The noise amplitude is denoted by αQ_0 in the figure legends.

4.5. Toward a More Complete Characterization of Small-Scale Fluctuations

Simulations conducted for this study use effectively constant noise realizations (Q_{small} not a function of time). However, for fully realistic auroras, one will also have time variability in the noise spectrum, though this is not well-constrained at this point. Indeed, fine-scale auroral imaging frequently reveals wave-like space-time structures that would have very distinctive signatures (Semeter & Blixt, 2006; Semeter et al., 2008). It seems plausible that such coherent structures could have a substantial impact on the production of ionization and, potentially, on attendant scintillation from these types of auroras.

More generally, there is a need to continue to use the narrow-field camera systems available to identify more events where there are concurrent ISR, camera, and scintillation measurements. The one event presented in this article has been helpful for making quantitative simulations; however, there are still some parameters (total energy flux and conjugate particle measurements from LEO spacecraft, like FAST) that are not well-constrained in this particular case. Having more individual event examples and analysis could help to better pin down the energy flux conditions under which the scintillation is occurring and types of spectral features at small scales that may also be associated. Further, if enough examples can be found, they will provide valuable information about the range of precipitation characteristics associated with the scintillation.

VAGGU ET AL. 16 of 19

4.6. Modeling Improvements

Construction of model inputs for event modeling (as opposed to noise-like characterizations used here) can be challenging as it is almost never the case that the model inputs can be fully specified with at least a few ad hoc assumptions required to convert data into fully 2D input particles and fields. However, recent progress (Clayton et al., 2019, 2021) does provide some potential pathways for event-realistic simulation and would seem to be a promising avenue moving forward.

While this study has focused exclusively on the effect of energetic electron precipitation on auroral scintillation, there is also a need to use models to examine the *combined* effects of these particles with various plasma instabilities. Auroral forms are known to be a source of sheared flow and strong plasma density gradients; thus, fluid instabilities like gradient-drift and Kelvin-Helmholtz should be examined more closely. A challenge here is that strong auroral precipitation, to our knowledge, has not been included in any prior instability simulations. So, there is little information on whether it may seed/suppress the progression other than the basic physical consideration that a completely uniform E-region will tend to short out charge accumulation associated with instabilities.

5. Conclusion

We utilize physics-based modeling to investigate how energetic electron precipitation generates density irregularities leading to radio scintillation. Our focus solely rests on modeling the density structures arising from impact ionization, excluding ionospheric electrodynamics. This approach isolates ionospheric structuring due to precipitation from external convection or instability-related effects. Our investigation centers on two key parameters—total energy flux (Q) and characteristic energies (E₀) and their impact on scintillation. Within the GEMINI model, we generate density structures by modifying precipitation flux, average energies, and the noise spectrum, integrated into precipitation that induces small-scale disturbances. Our exploration of this parameter space relies on observed data, including camera images detailing edge gradient scales, arc motion, arc width, and precipitation intensity in terms of both flux and energy in regions of scintillation, particularly in the vicinity of auroras. Utilizing the camera data, we characterize small-scale precipitation at a few hundred-meter scales, considering their spatial and temporal spectra within the camera's limitations. Additionally, we leverage PFISR Eregion density measurements in conjunction with the scintillation data for a comprehensive characterization. Narrow field camera data reveals a power law spectrum with a slope of -3 for small-scale features within auroral arcs, effectively capturing short-wavelength features crucial for generating scintillations. Incorporating this spectrum into our model allows us to explore its impact on scintillation by varying precipitation intensity and arc velocity. We design a non-uniform high-resolution grid with a resolution of ~ 100 m, which is utilized as the foundational framework to incorporate model inputs for generating plasma parameter profiles determined by the GEMINI chemistry. These precipitation-induced density structures from GEMINI are then imported into SIGMA, where we simulate and extract scintillation effects resulting from these structures.

Our simulations focus on various factors, as detailed in Table 1, including different precipitation energy fluxes, noise realizations with varying spectral indices, and arc motion, to explore their impact on radio scintillation.

Key findings from our analysis:

- 1. Energy Flux Impact: Higher energy fluxes (50 mW/m²) generate higher electron densities (1×10^{12} el/m³), resulting in more pronounced scintillation activity. The minimum energy level triggering scintillation is approximately ~7.5 mW/m².
- 2. Effect of Small-Scale Precipitation: Noise with a spectral slope of −5/3 induces stronger scintillation compared to a slope of −3, generating more turbulent spectra responsible for producing stronger scintillation effects.
- 3. Arc Motion Influence: The velocity of the auroral arc significantly affects scintillation. Higher arc velocities intensify refractive and diffractive (if small-scale features are present) effects, notably enhancing scintillation effects.
- 4. Irregularity Layers: Increasing the number of layers amplifies scintillation intensity. More number of layers expose the signal to multiple disruptions, intensifying scintillation effects.
- 5. Small-scale precipitation: The arc structure is a refractive medium, inducing phase-only fluctuations. Incorporating a power law noise spectrum over a finer grid resolution enables contributions to both phase and power variations introduced by long- and short-wavelength scale features.

VAGGU ET AL. 17 of 19

These findings contribute to a deeper understanding of how much small-scale precipitation is important for inducing scintillation and how factors such as the arc's energy and its motion influence the scintillation activity. These insights offer significant contributions for future studies focused on small-scale precipitation-associated scintillation, and in future simulations, we will probably want to resolve even more smaller-scale structures (within fluid model limits).

Data Availability Statement

GEMINI input configuration files, SIGMA time series outputs, and observational (camera) data used for this study are stored (Vaggu, 2024) and can be obtained at https://doi.org/10.5281/zenodo.11114475, https://doi.org/10.5281/zenodo.12169549. The SAGA scintillation data in Figure 11 is available at http://apollo.tbc.iit.edu/~spaceweather/live/. The GPS data in Figure 2 can be publicly accessible (registration required to access) at https://data.unavco.org/archive/gnss/, and the ASI data at http://optics.gi.alaska.edu/optics/realtime.

Acknowledgments

We (PV, MZ, and KD) acknowledge ERAU internal funds from the Center for Space and Atmospheric Research (CSAR), NSF CAREER Grants AGS-1848207, AGS-1255181, and NASA Grants NNX14AQ39G, and 80NSSC21K1354 for their support. The work of YN was supported by NASA Grants 80NSSC18K0657, 80NSSC20K0725, 80NSSC21K1321, 80NSSC22K0323, 80NSSC22K0749, 80NSSC22M0104, 80NSSC23K0410, NSF Grants AGS-1907698 and AGS-2100975, and AFOSR Grants FA9550-23-1-0634 and FA9550-23-1-0614. We thank ISSI Bern/ISSJ-BJ for the "Multi-Scale Magnetosphere-Ionosphere-Thermosphere Interaction" (project #511) team.

References

- Aarons, J., Lin, B., Mendillo, M., Liou, K., & Codrescu, M. (2000). Global positioning system phase fluctuations and ultraviolet images from the polar satellite. *Journal of Geophysical Research*, 105(A3), 5201–5213. https://doi.org/10.1029/1999ja900409
- Blelly, P., & Schunk, R. (1993). A comparative study of the time-dependent standard 8-, 13-and 16-moment transport formulations of the polar wind. In *Annales geophysicae* (Vol. 11, pp. 443–469).
- Buschmann, L. M., Bonnell, J. W., Bounds, S., Clausen, L., Kletzing, C., Marholm, S., et al. (2023). The role of particle precipitation on plasma structuring at different altitudes by in-situ measurements.
- Chartier, A., Forte, B., Deshpande, K., Bust, G., & Mitchell, C. (2016). Three-dimensional modeling of high-latitude scintillation observations. Radio Science, 51(7), 1022–1029. https://doi.org/10.1002/2015rs005889
- Clayton, R., Burleigh, M., Lynch, K. A., Zettergren, M., Evans, T., Grubbs, G., et al. (2021). Examining the auroral ionosphere in three dimensions using reconstructed 2D maps of auroral data to drive the 3D Gemini model. *Journal of Geophysical Research: Space Physics*, 126(11), e2021JA029749. https://doi.org/10.1029/2021ja029749
- Clayton, R., Lynch, K., Zettergren, M., Burleigh, M., Conde, M., Grubbs, G., et al. (2019). Two-dimensional maps of in situ ionospheric plasma flow data near auroral arcs using auroral imagery. *Journal of Geophysical Research: Space Physics*, 124(4), 3036–3056. https://doi.org/10.1020/2018/s026440
- Dahlgren, H., Semeter, J., Marshall, R., & Zettergren, M. (2013). The optical manifestation of dispersive field-aligned bursts in auroral breakup arcs. *Journal of Geophysical Research: Space Physics*, 118(7), 4572–4582. https://doi.org/10.1002/jgra.50415
- Datta-Barua, S., Su, Y., Deshpande, K., Miladinovich, D., Bust, G., Hampton, D., & Crowley, G. (2015). First light from a kilometer-baseline scintillation auroral GPS array. Geophysical Research Letters, 42(10), 3639–3646. https://doi.org/10.1002/2015gl063556
- Deshpande, K., Bust, G., Clauer, C., Rino, C., & Carrano, C. (2014). Satellite-beacon ionospheric-scintillation global model of the upper atmosphere (sigma) I: High-latitude sensitivity study of the model parameters. *Journal of Geophysical Research: Space Physics*, 119(5), 4026–4043. https://doi.org/10.1002/2013ja019699
- Deshpande, K., Bust, G., Clauer, C., Scales, W., Frissell, N., Ruohoniemi, J., et al. (2016). Satellite-beacon ionospheric-scintillation global model of the upper atmosphere (sigma) II: Inverse modeling with high-latitude observations to deduce irregularity physics. *Journal of Geophysical Research: Space Physics*, 121(9), 9188–9203. https://doi.org/10.1002/2016ja022943
- Deshpande, K. B., & Zettergren, M. D. (2019). Satellite-beacon ionospheric-scintillation global model of the upper atmosphere (sigma) III: Scintillation simulation using a physics-based plasma model. *Geophysical Research Letters*, 46(9), 4564–4572. https://doi.org/10.1029/2019g1082576
- Diloy, P.-Y., Robineau, A., Lilensten, J., Blelly, P.-L., & Fontanari, J. (1996). A numerical model of the ionosphere, including the e-region above eiscat. In *Annales geophysicae* (Vol. 14, pp. 191–200). https://doi.org/10.1007/s00585-996-0191-7
- Evans, D. S. (1974). Precipitating electron fluxes formed by a magnetic field aligned potential difference. *Journal of Geophysical Research*, 70(10), 2853, 2859. https://doi.org/10.1020/is070010p02853
- 79(19), 2853–2858. https://doi.org/10.1029/ja079i019p02853
 Fang, X., Randall, C. E., Lummerzheim, D., Solomon, S. C., Mills, M. J., Marsh, D. R., et al. (2008). Electron impact ionization: A new
- parameterization for 100 ev to 1 mev electrons. *Journal of Geophysical Research*, 113(A9), A09311. https://doi.org/10.1029/2008ja013384 Hosokawa, K., Otsuka, Y., Ogawa, Y., & Tsugawa, T. (2014). Observations of GPS scintillation during an isolated auroral substorm. *Progress in Earth and Planetary Science*, 1(1), 1–9. https://doi.org/10.1186/2197-4284-1-16
- Jayachandran, P., Hosokawa, K., MacDougall, J., Mushini, S., Langley, R., & Shiokawa, K. (2009). GPS total electron content variations associated with a polar cap arc. *Journal of Geophysical Research*, 114(A12), A12304. https://doi.org/10.1029/2009ja014916
- Jayachandran, P., Hosokawa, K., Shiokawa, K., Otsuka, Y., Watson, C., Mushini, S., et al. (2012). GPS total electron content variations associated with poleward moving sun-aligned arcs. *Journal of Geophysical Research*, 117(A5), 21. https://doi.org/10.1029/2011ja017423
- Jin, Y., Moen, J. I., & Miloch, W. J. (2014). GPS scintillation effects associated with polar cap patches and substorm auroral activity: Direct comparison. Journal of Space Weather and Space Climate, 4, A23. https://doi.org/10.1051/swsc/2014019
- Kaeppler, S., Nicolls, M., Strømme, A., Kletzing, C., & Bounds, S. (2014). Observations in the e region ionosphere of kappa distribution functions associated with precipitating auroral electrons and discrete aurorae. *Journal of Geophysical Research: Space Physics*, 119(12), 10–164. https://doi.org/10.1002/2014ja020356
- Karlsson, T. (2012). The acceleration region of stable auroral arcs. In Chapman conference on the relationship between auroral phenomenology and magnetospheric processes, Feb 27-Mar 04, 2011, Fairbanks, AK (pp. 227–239).
- Kelley, M. C., Vickrey, J. F., Carlson, C., & Torbert, R. (1982). On the origin and spatial extent of high-latitude F region irregularities. *Journal of Geophysical Research*, 87(A6), 4469–4475. https://doi.org/10.1029/ja087ia06p04469
- Kintner, P. M., Ledvina, B. M., & De Paula, E. (2007). GPS and ionospheric scintillations. Space Weather, 5(9), S09003. https://doi.org/10.1029/2006sw000260
- Kintner, P. M., & Seyler, C. E. (1985). The status of observations and theory of high latitude ionospheric and magnetospheric plasma turbulence. Space Science Reviews, 41(1-2), 91–129. https://doi.org/10.1007/bf00241347

VAGGU ET AL. 18 of 19

21699402,

- Lamarche, L. J., Deshpande, K. B., & Zettergren, M. D. (2022). Observations and modeling of scintillation in the vicinity of a polar cap patch. Journal of Space Weather and Space Climate, 12, 27. https://doi.org/10.1051/swsc/2022023
- Loucks, D., Palo, S., Pilinski, M., Crowley, G., Azeem, I., & Hampton, D. (2017). High-latitude GPS phase scintillation from e region electron density gradients during the 20–21 December 2015 geomagnetic storm. *Journal of Geophysical Research: Space Physics*, 122(7), 7473–7490. https://doi.org/10.1002/2016ja023839
- McIntosh, R., & Anderson, P. (2014). Maps of precipitating electron spectra characterized by Maxwellian and Kappa distributions. *Journal of Geophysical Research: Space Physics*, 119(12), 10–116. https://doi.org/10.1002/2014ja020080
- Moen, J., Oksavik, K., Alfonsi, L., Daabakk, Y., Romano, V., & Spogli, L. (2013). Space weather challenges of the polar cap ionosphere. *Journal of Space Weather and Space Climate*, 3, A02. https://doi.org/10.1051/swsc/2013025
- Morooka, M., Mukai, T., & Fukunishi, H. (2004). Current-voltage relationship in the auroral particle acceleration region. In *Annales geophysicae* (Vol. 22, pp. 3641–3655). https://doi.org/10.5194/angeo-22-3641-2004
- Mrak, S., Semeter, J., Hirsch, M., Starr, G., Hampton, D., Varney, R. H., et al. (2018). Field-aligned GPS scintillation: Multisensor data fusion. Journal of Geophysical Research: Space Physics, 123(1), 974–992. https://doi.org/10.1002/2017ja024557
- Nishimura, Y., Kelly, T., Jayachandran, P., Mrak, S., Semeter, J. L., Donovan, E., et al. (2023). Nightside high-latitude phase and amplitude scintillation during a substorm using 1-second scintillation indices. *Journal of Geophysical Research: Space Physics*, 128(8), e2023JA031402. https://doi.org/10.1029/2023ja031402
- Nishimura, Y., Lyons, L., Gabrielse, C., Sivadas, N., Donovan, E., Varney, R., et al. (2020). Extreme magnetosphere-ionosphere-thermosphere responses to the 5 April 2010 supersubstorm. *Journal of Geophysical Research: Space Physics*, 125(4), e2019JA027654. https://doi.org/10.1029/2019ja027654
- Ogasawara, K., Asamura, K., Takashima, T., Saito, Y., & Mukai, T. (2006). Rocket observation of energetic electrons in the low-altitude auroral ionosphere during the delta campaign. *Earth Planets and Space*, 58(9), 1155–1164. https://doi.org/10.1186/bf03352005
- Richards, P., Fennelly, J., & Torr, D. (1994). Euvac: A solar EUV flux model for aeronomic calculations. *Journal of Geophysical Research*, 99(A5), 8981–8992. https://doi.org/10.1029/94ja00518
- Rino, C. (2011). The theory of scintillation with applications in remote sensing. John Wiley & Sons.
- Rino, C. L., & Carrano, C. S. (2011). The application of numerical simulations in beacon scintillation analysis and modeling. *Radio Science*, 46(03), 1–10. https://doi.org/10.1029/2010rs004563
- Schunk, R. W., & Sojka, J. J. (1997). Global ionosphere-polar wind system during changing magnetic activity. *Journal of Geophysical Research*, 102(A6), 11625–11651. https://doi.org/10.1029/97ja00292
- Semeter, J., & Blixt, E. (2006). Evidence for Alfvén wave dispersion identified in high-resolution auroral imagery. *Geophysical Research Letters*, 33(13), L13106. https://doi.org/10.1029/2006gl026274
- Semeter, J., Mrak, S., Hirsch, M., Swoboda, J., Akbari, H., Starr, G., et al. (2017). GPS signal corruption by the discrete aurora: Precise measurements from the Mahali experiment. Geophysical Research Letters, 44(19), 9539–9546. https://doi.org/10.1002/2017g1073570
- Semeter, J., Zettergren, M., Diaz, M., & Mende, S. (2008). Wave dispersion and the discrete aurora: New constraints derived from high-speed imagery. *Journal of Geophysical Research*, 113(A12), 12208. https://doi.org/10.1029/2008ja013122
- Solomon, S. C. (2017). Global modeling of thermospheric airglow in the far ultraviolet. *Journal of Geophysical Research: Space Physics*, 122(7), 7834–7848. https://doi.org/10.1002/2017ja024314
- Solomon, S. C., & Qian, L. (2005). Solar extreme-ultraviolet irradiance for general circulation models. *Journal of Geophysical Research*, 110(A10), A10306. https://doi.org/10.1029/2005ja011160
- Spicher, A., Deshpande, K., Jin, Y., Oksavik, K., Zettergren, M. D., Clausen, L. B., et al. (2020). On the production of ionospheric irregularities via kelvin-Helmholtz instability associated with cusp flow channels. *Journal of Geophysical Research: Space Physics*, 125(6), e2019JA027734, https://doi.org/10.1029/2019ja027734
- Sreenivash, V., Su, Y., & Datta-Barua, S. (2020). Automated ionospheric scattering layer hypothesis generation for detected and classified auroral global positioning system scintillation events. *Radio Science*, 55(1), e2018RS006779. https://doi.org/10.1029/2018rs006779
- St.-Maurice, J.-P., & Laneville, P. (1998). Reaction rate of O⁺ with O₂, N₂, and no under highly disturbed auroral conditions. *Journal of Geophysical Research*, 103(A8), 17519–17521. https://doi.org/10.1029/98ja01387
- Vaggu, P. R. (2024). Model-based investigation of electron precipitation-driven density structures and their effects on auroral scintillation [Dataset]. Zenodo. https://doi.org/10.5281/zenodo.11114475
- Vaggu, P. R., Deshpande, K. B., Datta-Barua, S., Bust, G. S., Hampton, D. L., Rubio, A. L., & Conroy, J. P. (2023). Morphological and spectral features of ionospheric structures at e-and f-region altitudes over poker flat analyzed using modeling and observations. Sensors, 23(5), 2477. https://doi.org/10.3390/s23052477
- Wang, Y., Cao, Z., Xing, Z.-Y., Zhang, Q.-H., Jayachandran, P. T., Oksavik, K., et al. (2021). GPS scintillations and TEC variations in association with a polar cap arc. *Journal of Geophysical Research: Space Physics*, 126(3), e2020JA028968. https://doi.org/10.1029/2020ja028968
- Weber, E., Buchau, J., Moore, J., Sharber, J., Livingston, R., Winningham, J. D., & Reinisch, B. (1984). F layer ionization patches in the polar cap. Journal of Geophysical Research, 89(A3), 1683–1694. https://doi.org/10.1029/ja089ia03p01683
- Yeh, K. C., & Liu, C.-H. (1982). Radio wave scintillations in the ionosphere. *Proceedings of the IEEE*, 70(4), 324–360. https://doi.org/10.1109/proc.1982.12313
- Zettergren, M., Lynch, K., Hampton, D., Nicolls, M., Wright, B., Conde, M., et al. (2014). Auroral ionospheric f region density cavity formation and evolution: Mica campaign results. *Journal of Geophysical Research: Space Physics*, 119(4), 3162–3178. https://doi.org/10.1002/2013ja019583
- Zettergren, M., & Semeter, J. (2012). Ionospheric plasma transport and loss in auroral downward current regions. *Journal of Geophysical Research*, 117(A6), 6306. https://doi.org/10.1029/2012ja017637
- Zettergren, M., & Snively, J. (2015). Ionospheric response to infrasonic-acoustic waves generated by natural hazard events. *Journal of Geophysical Research: Space Physics*, 120(9), 8002–8024. https://doi.org/10.1002/2015ja021116

VAGGU ET AL. 19 of 19